

Corso di Laurea magistale in Fisica (LM-17)



UNIVERSITÀ DEGLI STUDI DI MILANO
FACOLTÀ DI SCIENZE E TECNOLOGIE

Dipartimento di Fisica “Aldo Pontremoli”

**Implementation and simulation of
the pointing reconstruction model for
the LSPE/Strip telescope.**

Relatore:
Prof. Maurizio TOMASI
Correlatore:
Dott. Michele MARIS

Tesi di Laurea di:
Matteo BARATTO
Matricola: 983675

Anno Accademico 2021/2022

Abstract

The “Large Scale Polarization Explorer” (LSPE) is an experiment dedicated to the study of the polarization of the CMB. It is composed of two instruments: *SWIPE*, a stratospheric balloon, and *Strip*, a ground based telescope. My thesis was carried out within the framework of LSPE/*Strip*. The latter, once operational, will be placed at the Teide Astronomical Observatory in Tenerife, and will observe the polarized sky signal at the frequencies of 43 GHz and 90 GHz carrying out a survey of about 25% of the sky.

LSPE/*Strip* is currently under development and the aim of this thesis is the analysis of the impact that systematic errors could have in the reconstruction of the LSPE/*Strip* telescope pointing. Currently, the prerequisite for pointing accuracy is 30 arcsec. The simulations I carried out will serve to establish if it is possible to relax this prerequisite to 1 arcmin.

The errors I have considered are due to uncertain knowledge on the *configuration angles* describing the geometric model of the telescope: the offset on the altitude motor, the offset on the azimuth motor, the fork angle, and the wobble angles.

Starting from the geometric model, I expanded the official LSPE/*Strip* simulation pipeline (*Stripline.jl*) by introducing the possibility of simulating non-idealities in these angles. I have assumed that the geometry of the telescope is described only by the *configuration angles*, which are assumed constant (no aging or time-dependent flexures) apart from the azimuth, as the telescope will spin at a constant angular speed during nominal operations.

Firstly, I analyzed the actual pointing error, intended as the angular deviation between the ideal direction and the one effectively obtained by introducing a perturbation on the configuration angles other than zero. I analyzed the configuration angles individually, and obtained that, for small uncertainties, the pointing error scales linearly with the value assigned to the configuration angle: the altitude motor offset turns out to be the most problematic with an approximately one-to-one dependence, then the azimuth motor offset, and the fork angle follow; the wobble angles, on the other hand, always remain below the minimum prerequisite.

After that, I increased the complexity of the simulation by introducing a realistic sky signal to be observed (synchrotron with constant spectral index) and I studied how a bias of 1 arcmin introduced in one of the configuration angles could distort the observed signal. In this case, I produced sky maps containing the signal observed by LSPE/*Strip* both in the ideal case and in the case affected by this pointing error. By subtracting the map with the error from the ideal one, I obtained the so-called *error maps*, whose pixel values follow a Cauchy distribution. The width of the distribution scales linearly with the perturbation introduced in the configuration angles for the motor offsets and for the fork angle, but it follows a power law with index ≈ 2 for the wobble angles. Despite this, in the range of interest of 1 arcmin, wobble angles cause a lower error than in the former cases. In the worst case, the error distribution has a width of the order of $10^{-3}\mu\text{K}$, thus orders of magnitude lower than instrumental sensitivity ($130\ \mu\text{K}/\text{arcmin}^2$ at 43 GHz).

Finally, I performed a component separation introducing the pointing error on LSPE/*Strip* generated maps. Component separation allows, given a sky model and a series of maps at various observed frequencies, to fit the characteristic parameters of

the foregrounds for each pixel of the map; thus allowing to separate the components that make up the observed signal: specifically, in my thesis I chose a realistic sky model formed by CMB, synchrotron and dust.

I considered two cases: in the first, I used only the frequency bands covered by the LSPE project, in the second case, instead, I also added the bands covered by *WMAP*, *Planck* and *Quijote*. As a use case, I analyzed how much the pointing error distorted the synchrotron spectral index fitted during component separation. To evaluate the impact of pointing error, I assumed that a systematic error is negligible if its effect is below 10% of the effect of the white noise level of the detectors.

For uncertainties in the configuration angles of the order of 1 arcmin, the results show that the impact of pointing error is below the 10% threshold. For greater uncertainties the most problematic parameter is the fork angle when only LSPE is considered, while in the other case it is the offset on the altitude angle: it will therefore be necessary to pay particular attention to the calibration of these parameters.

In conclusion, given the results obtained in the study of the distribution of the absolute pointing error in the maps and given the result of the component separation, it is possible to state that the requirement on the pointing accuracy of LSPE/Strip can be increased from 0.5 arcmin up to 1 arcmin with a negligible impact in the characterization of the Galactic diffuse synchrotron emission.

Contents

I	Introduction	2
1	Cosmic Microwave Background	3
1.1	The Standard Cosmological Model	3
1.2	Relic radiation	4
1.2.1	Black body spectrum	5
1.2.2	CMB Polarization	5
2	Large-Scale Polarization Explorer	7
2.1	LSPE/Strip	7
2.2	Scanning strategy	8
2.3	Star tracker	9
3	Pointing Reconstruction Method	10
3.1	Non idealities angles	10
3.2	Pointing Reconstruction Model	11
II	Simulations	14
4	Simulations setup	15
4.1	Simulation pipeline	15
4.1.1	TOD and binned maps	16
4.2	Sky model	17
4.2.1	CMB	17
4.2.2	Dust	17
4.2.3	Synchrotron	18
5	Simulations results	20
5.1	Pointing accuracy	20
5.2	Simulation duration	21
5.3	Noise maps and histograms	22
5.4	Error scaling	24
6	Component separation analysis	26
6.1	Results using only LSPE	28
6.2	Results with other instruments	29
7	Conclusions	32
A	Linearization	34

Part I

Introduction

Chapter 1

Cosmic Microwave Background

The Cosmic Microwave Background (CMB) is electromagnetic radiation produced in the early stage of the universe that permeates the entire observable Universe. It is a quasi-isotropic radiation with a black-body spectrum at a temperature of $T \approx 2.73\text{ K}$ and a number density of photon $n_\gamma \approx 400\text{ cm}^{-3}$. Predicted in 1948 by R. Alpher et al. it was first observed by A. Penzias and R.W. Wilson in 1965 using the antenna of the Holmdel observatory in New Jersey. [10]

In this chapter, I will first present an introduction to the standard cosmological model (Section 1.1) to understand better the origin and the features of CMB (Section 1.2). Then, I will discuss CMB polarization (Section 1.2.2), which is the main observational goal of the LSPE project.

1.1 The Standard Cosmological Model

The Standard Cosmological Model is a framework that describes the evolution of the Universe from an initial singularity called the Big Bang. The model assumes that the Universe is homogeneous and isotropic (*cosmological principle*) and that it is expanding at a rate that depends on the matter type and energy it is composed of.

As first discovered by Hubble [5], galaxies are receding from us with an apparent recession velocity which increases linearly with the distance:

$$v = H_0 d \tag{1.1}$$

where H_0 is the *Hubble constant*, which value has been measured with many different techniques [4]. Below, is the result obtained by Planck Collaboration [11]:

$$H_0 = 67.4 \pm 0.5 \text{ km s}^{-1} \text{ Mpc}^{-1}$$

This has been one of the first pieces of evidence that suggested that the Universe is expanding. To better study the expansion's dynamic, it is useful to adopt a co-moving coordinate system. The physical distance $r(t)$, called *proper distance*, can be written in terms of a *co-moving coordinate* and a *scale factor* which depends on time:

$$r(t) = a(t)x \quad \text{with} \quad a(t_{\text{now}}) = 1, \quad \dot{a}(t) > 0 \tag{1.2}$$

Taking the derivative of the previous equation, we find a more precise form of the Hubble law:

$$v(r, t) = \dot{r}(t) = \dot{a}(t)x = \frac{\dot{a}(t)}{a(t)}r \equiv H(t)r \tag{1.3}$$

in which we have defined the *Hubble parameter* (its value at time $t = t_{\text{now}}$ is the Hubble constant). The Hubble parameter describes the Universe's evolution and can be linked to observations not only through the Hubble constant but also with the Universe's composition and structure. Solving Einstein's equation with the Friedmann-Lemaître-Robertson-Walker metric leads to two equations describing the evolution of the scale factor:

$$\left(\frac{\dot{a}(t)}{a(t)}\right)^2 = \frac{8\pi G}{3c^2}\rho(t) - \frac{kc^2}{a^2(t)} \quad (1.4)$$

$$\frac{\ddot{a}(t)}{a(t)} = -\frac{4\pi G}{3c^2} \left(\rho(t) + \frac{3p(t)}{c^2} \right) \quad (1.5)$$

where k is the curvature parameter, $\rho(t)$ is the energy density, and $p(t)$ is the pressure associated with the three components of the Universe: matter, radiation, and dark energy. Taken $k = 0$ (Euclidean space) it is possible to define a critical density that represents the threshold between a positively curved space and a negatively curved one:

$$\rho_c(t) = \frac{3c^2}{8\pi G}H^2(t) \quad (1.6)$$

and then the *density parameters*:

$$\Omega_i(t) = \frac{\rho(t)}{\rho_c(t)} \quad (1.7)$$

where i represent the three possible component of matter $\{m, \gamma, \Lambda\}$. Using these adimensional parameters leads to the following equation:

$$H^2(t) = H_0^2 \left[\frac{\Omega_\gamma(t_{\text{now}})}{a^4(t)} + \frac{\Omega_m(t_{\text{now}})}{a^3(t)} + \frac{1 - \Omega_0}{a^2(t)} + \Omega_\Lambda(t_{\text{now}}) \right] \quad (1.8)$$

where Ω_0 is related to the total curvature of the space-time through $kc^2 = H_0^2(\Omega_0 - 1)$. This equation shows that the evolution of the scale factor depends on the density parameters at the present times, pointing out the importance of the measurements of the latter.

Therefore, due to the expansion of the Universe, going back in time, we expect that the Universe was denser and hotter and from Eq. 1.8 that the early Universe ($a \ll 1$) was dominated by radiation. It is in this scenario that CMB originated; in the next section I will present a brief history of the Universe until the recombination era and I will discuss the main features of the *relic radiation*.

1.2 Relic radiation

According to the inflationary paradigm and the Big Bang theory, the Universe started to expand and cool from a hot and high-density singularity. At $t = 0$, immediately after the Big Bang, the Universe underwent a rapid expansion called inflation that flattened out inhomogeneities in the primordial plasma. After the inflationary epoch (which lasted about 10^{-33} s), the expansion of the Universe continued at a slower rate. This expansion was followed by a progressive temperature drop: the reduced energy permitted the transition from an initial hot quark-gluon

plasma to a hadron-composed plasma, in which matter and radiation were in thermal equilibrium thanks to Thomson scattering. This means that all the species had the same temperature and it is possible to talk of the temperature of the Universe. This era of equilibrium ended when the temperature drops below $T \approx 3000\text{ K}$ when nuclei and electrons became to combine forming neutral atoms; the number density of electrons went to zero and the mean free path of photons diverged.

The moment in which the mean free path of photons becomes larger than the scale of the observable universe is called *decoupling* ($t_{\text{dec}} \approx 380\,000\text{ yrs}$): at this moment, the Universe became transparent to radiation and the photons began to freely propagate through space. This is the moment in which the *Cosmic Microwave Background* was formed. The decoupling is assumed to have occurred everywhere at about the same time: we can observe only the photons that have been scattered toward the Earth, more precisely the ones produced on a spherical shell with a radius $d_{\text{LSS}} = c(t_{\text{now}} - t_{\text{dec}})$ called *Last Scattering Surface*.

1.2.1 Black body spectrum

The number density of photons in equilibrium with the matter at temperature T is given by a black-body spectrum defined for a frequency range $[\nu, \nu + d\nu]$ as follows:

$$n_T(\nu)d\nu = \frac{8\pi\nu^2d\nu}{\exp(h\nu/k_bT) - 1}. \quad (1.9)$$

It is possible to demonstrate that under a free expansion, like the one encountered by photons after decoupling, the spectrum keeps the same form with only a modified temperature:

$$T(t) = T(t_{\text{LSS}}) \frac{a(t_{\text{LSS}})}{a(t)} \quad (1.10)$$

where $a(t)$ is the scale factor discussed in Section 1.1.

Today we observe CMB at a temperature of about $T \approx 2.73\text{ K}$ with a density of photon $n_\gamma \approx 400\text{ cm}^{-3}$. [3]

1.2.2 CMB Polarization

Thomson scattering, which took photons and electrons in thermal equilibrium before the decoupling, preserves the polarization direction of the incoming radiation. This is an elastic scattering between a photon and a charged particle: the electron, hit by a polarized photon, starts to oscillate along the polarization direction and emit a polarized electromagnetic radiation whose intensity is proportional to:

$$\frac{dP}{d\Omega}(\hat{r}) = \left(\frac{q^2}{4\pi\epsilon_0 mc^2} \right)^2 \frac{\epsilon_0 c E_0^2}{2} \sin^2 \theta \quad (1.11)$$

where E_0 is the amplitude of the incoming radiation and θ the angle between \hat{r} and the polarization direction. For a superposition of several randomly oriented plane waves, the scattered radiation is not polarized because the polarization induced by each wave is averaged out: if the incoming radiation were isotropic, orthogonal polarization states (separated by 90°) would balance so that the outgoing radiation would remain unpolarized.

Nevertheless, if the radiation field around an electron has a quadrupolar component, representing a variation on an angle of 90° , polarization can arise from scattering. Quadrupoles can be described by Laplace's spherical harmonics $Y_l^m(\theta, \phi)$ with $l = 2$ and $m = 0, \pm 1, \pm 2$. At every possible value of $|m|$ corresponds a different perturbation that can generate a quadrupole pattern in the radiation:

- adiabatic pressure oscillation (sound waves) produces quadrupoles with $m = 1$,
- vorticity in the velocity field produces quadrupoles with $m = \pm 1$,
- gravitational waves produce quadrupoles with $m = \pm 2$.

The polarization field of the CMB can be decomposed into spherical harmonics. Taking the second rank traceless tensor:

$$P_{ab} = \begin{pmatrix} Q & U \\ U & -Q \end{pmatrix}, \quad (1.12)$$

where Q and U are the Stokes parameters that characterize the linear polarization, the polarization tensor Eq. 1.12 can be decomposed in spherical harmonics using a gradient field E and a curl field B :

$$P_{ab}(\theta, \phi) = \sum_{l=0}^{\infty} \sum_{m=-l}^l (a_{lm}^E Y_{(lm)ab}^E + a_{lm}^B Y_{(lm)ab}^B). \quad (1.13)$$

The analysis of polarization data requires measuring Q and U and then producing a sky map to convert to E and B modes. B-modes can only be produced by a perturbation generated by primordial gravitational waves during inflation, the main problem is that the amount of power associated with B-modes is significantly smaller than the power in E-modes. To quantify this gap, it is common to use the tensor-to-scalar ratio r , quantifying the ratio between B-modes and E-modes power. Today we have set an upper limit to this value [16] of about $r < 0.044$ with a 95% CL.

Chapter 2

Large-Scale Polarization Explorer

The Large Scale Polarization Explorer (LSPE) is a project funded by the Italian Space Agency (ASI) and by the Istituto Nazionale di Fisica Nucleare (INFN). It comprises two experiments: a ground-based telescope called STRIP and a balloon-borne mission called SWIPE that will observe the sky at 145, 210, and 240 GHz in a winter arctic stratospheric flight. The two experiments will observe serve approximately the same sky covering about 30% of the Northern Sky.

The main goal of LSPE is to constrain the tensor-to-scalar ratio to $r \approx 0.03$ at a 99.7% confidence level [1] and, more generally, to study the polarized emission of the Milky Way produced by synchrotron and interstellar dust emission.

In the next section, I will present LSPE/Strip experiment (Sec. 2.1) focusing specifically on its scanning strategy (Sec. 2.2) and on the star tracker (Sec. 2.3), used for the pointing reconstruction.

2.1 LSPE/Strip

LSPE/Strip [2] is a ground-based coherent polarimeter array that will be placed at the Teide Observatory in Tenerife. It will observe the sky in two frequency bands centered at 43 GHz (Q-band) and 95 GHz (W-band) through a dual reflector crossed-Dragone telescope with a 1.5 m aperture. In particular, the polarimeter's design allows Strip to directly measure the Stokes Q and U components.

The 95 GHz channel (composed of 6 detectors), due to its poor sensitivity, is not able to detect alone the astrophysical signal and it will be used to study the atmospheric emission both in intensity and in polarization. On the other hand, the 43 GHz channel (composed of 49 detectors) is the one properly devoted to measuring Galactic synchrotron emission, since this is the dominant foreground emission at that frequency. These measurements, combined with lower frequency data from other surveys, are crucial to constrain synchrotron parameters.

The optical assembly is installed on top of an alt-azimuth mount, which allows the rotation of the telescope around two perpendicular axes to change the azimuth and elevation angle (Fig. 2.1); each motor is equipped with an absolute encoder that returns the angle at which the two axes are rotated with respect to the reference directions: the north and the horizon (or the zenith). In Sec. 2.2 it is presented how these motors intervene in the scanning strategy of the telescope.

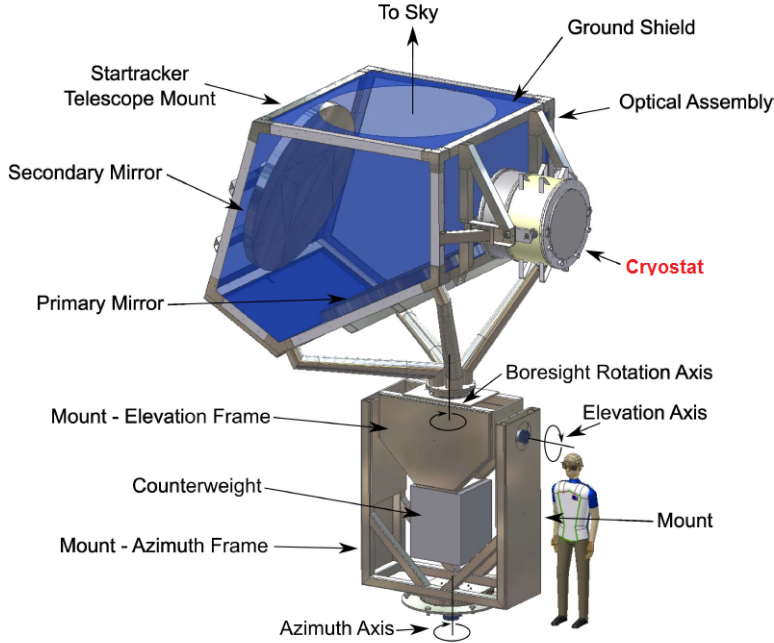


Figure 2.1: LSPE/Strip telescope system overview.

LSPE/Strip sensitivity can be quantified in terms of map sensitivity:

$$\sigma_{Q,U}^2 = \text{NET}^2 \frac{4\pi f_{\text{sky}}}{T_{\text{obs}} N_{\text{det}}} \quad (2.1)$$

where T_{obs} is the effective integration time, NET is the noise equivalent temperature of each detector, f_{sky} is the observed sky fraction, and N_{det} is the number of detectors. As reported in [1] the sensitivity of LSPE/Strip is:

	43 GHz	95 GHz
Map sensitivity [μK_{CMB} arcmin]	102	777

2.2 Scanning strategy

The LSPE/Strip telescope performs a regular, uninterrupted movement using the *azimuth motor*, which makes the whole structure spin around its gravity axis at 1 rpm; as a result, the telescope will describe circles on the sky whose radius depends on the zenithal angle θ . The altitude of the telescope can be varied using the *altitude motor*, to adjust the fraction of sky observed by the telescope. The motion of the telescope, coupled with the Earth's rotation, allows the scanning of a strip in the sky with equatorial declination δ ranging $\text{lat}_{\text{tel}} - \theta < \delta < \text{lat}_{\text{tel}} + \theta$, where $\text{lat}_{\text{tel}} \approx 28^\circ 18' \text{ N}$ is Tenerife latitude (Fig. 2.2).

The final altitude is chosen as a trade-off between the sky coverage (in order to maximize the overlap with LSPE/SWIPE) and the noise per pixel distribution. In fact, the greater the zenithal angle the wider the observed strip of the sky will be; at the same time (if the time span of the observation remains unchanged) the

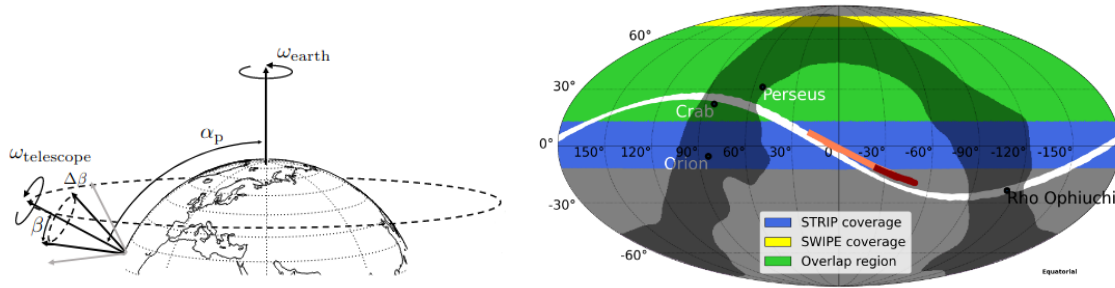


Figure 2.2: *Left:* Strip combines motion around its own axis and around Earth’s axis; *Right:* sky coverage and overlap region of Strip (at a zenithal angle $\theta = 35^\circ$) and SWIPE. Both are taken from [1].

single-pixel error will be greater because it will be observed fewer times. In this thesis, I will use a value of $\theta = 20^\circ$ that ensures an overlap of about the 80% with SWIPE and satisfy the STRIP sensitivity [6].

2.3 Star tracker

To project the observed signal onto a map, it is necessary to know where, at each time, the telescope is pointing in the sky (Ch. 3). As mentioned in the previous section (Sec. 2.1), LSPE/Strip is a polarimeter and will measure only Q and U Stokes components; at 43 GHz (Q-band) there are only a few bright polarized sources that can be used to calibrate the pointing direction (Crab Nebula, Perseus, as well as the Moon [6]). To improve the pointing reconstruction accuracy, it is necessary to use an optical device that measures the direction toward which the telescope is aimed by looking at the position of the stars, a so-called *star tracker*: in this way, radio and optical observations will be used to reconstruct the pointing direction.

The star tracker reconstructs its pointing direction by measuring the apparent positions of known stars; from a mathematical point of view, given (u, v) a system of coordinates in the image plane observed by the star tracker, determining the pointing direction $\hat{\mathbf{P}}$ and the camera orientation angles¹ $(p_{\text{sr}}, r_{\text{sr}}, t_{\text{sr}})$ is equivalent to determine the projector operator $\mathcal{A}(\hat{\mathbf{P}}, p_{\text{sr}}, r_{\text{sr}}, t_{\text{sr}})$ of an observed star given its position $\hat{\mathbf{P}}_*$ and the observed image position $(u_*, v_*) = \mathcal{A} \cdot \hat{\mathbf{P}}_*$.

The LSPE/Strip project requires a pointing accuracy of at least 30 arcsec (15 arcsec in the best case, with the use of the star tracker) [1]; in the next chapters I will investigate whether the project design, with its non-idealities, allows achieving this precision and whether the requirement can be relaxed.

¹Tait-Bryan angles encoding the position of the camera with respect to the telescope focal plane (See Ch.3).

Chapter 3

Pointing Reconstruction Method

As anticipated in Sec. 2.3, to reconstruct the observed signal, it is necessary to know, at each time, where LSPE/Strip is pointing. The Pointing Reconstruction Method (PRM) is the process of deriving the aiming direction of the telescope's detector using the information provided by the Telescope Control Station (for example, the angles measured by the encoders paired with the telescope motors, see Sec. 2.1) and the information available on the telescope geometry encoded in a set of *configuration angles* determined, as an example, by using the Star tracker. [7]

In this chapter, I will discuss the telescope geometry (Sec. 3.1), and then I will present the model used by the pointing reconstruction pipeline (Sec. 3.2).

3.1 Non idealities angles

LSPE/Strip will be installed on an alt-azimuth mount, allowing the instrument to rotate around a vertical axis using the *altitude motor* and around a horizontal axis using the *azimuth motor*; the two *control angles* encoding the positions of the latter motors are not enough to completely reconstruct the direction of sight of the telescope (Sec. 3.2). It is essential to define a geometrical model that considers different *configuration angles* encoding the geometry of the telescope and its non-idealities. It is important to underline that the geometry of the system is well-defined and time-independent, consequently, flexures and aging are not considered.

A simplified model is reported in Fig. 3.1: a flat base holds a vertical axis (V-AXIS) allowing the azimuth rotation and, on top of that, is placed a fork along a horizontal axis (H-AXIS) allowing the altitude rotation. In the ideal case, the V-AXIS is perpendicular to the H-AXIS and is aligned with the local topocentric zenith. The fork holds the focal plane of the telescope, in which the detectors are placed; in general, every device connected with the telescope that collects electromagnetic radiation is labeled as *camera* and its orientation (with respect to the focal plane) can be described through three Tait-Bryan angles ($p_{\text{cam}}, t_{\text{cam}}, r_{\text{cam}}$) representing an anticlockwise rotation around $(\hat{e}_x, \hat{e}_y, \hat{e}_z)$ axis.

Let's define θ as the angle at which the altitude motor is located (the case $\theta = 0$ corresponds to the instrument looking along the zenith) and ϕ the angle at which the azimuth motor is located, together with the angles which define the direction of the camera we need five more *configuration angles* to fully describe the non-ideal system [7]:

- $[\theta_0, \varphi_0]$: zero points (offsets) of the encoders that measure the *control angles*;

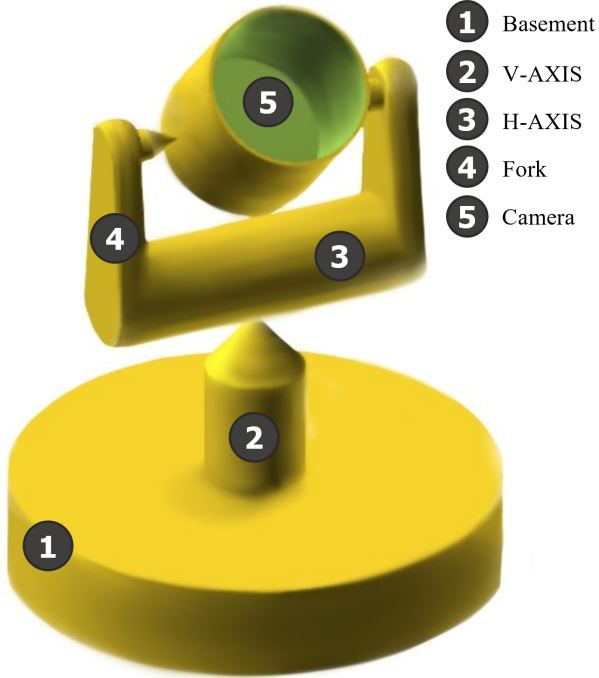


Figure 3.1: Simplified model of the Alt-Azimuth telescope.

- t_{fork} : measures the misalignment of the fork i.e., the non-perpendicularity between V-AXIS and H-AXIS;
- $[z_{\text{Vax}}, \omega_{\text{Vax}}]$: encodes the deviation of the V-AXIS from the local topocentric zenith; z_{Vax} is the angle between V-AXIS and the zenith while ω_{Vax} is the direction of the tilt measured as the azimuth of the ascending node.

In the next section, we will see how these angles affect the calculation of the pointing direction.

3.2 Pointing Reconstruction Model

To reconstruct the aiming direction of an observer located in a given place at a given time, it is necessary to determine the direction of sight \mathbf{P} with respect to the local topocentric reference frame and then project it into the Celestial Equatorial reference frame. Firstly, let's define three different reference frames (all of that are right-handed and with positive angles defined by anticlockwise rotations):

- Topocentric Horizontal r.f.: the origin is in the observer location (defined by latitude, longitude, and height above the sea level) with \hat{e}_x oriented towards South, \hat{e}_y oriented towards East and \hat{e}_z defined by the local zenith;
- Telescope r.f.: the origin is in the center of the focal plane with \hat{e}_x coinciding with H-AXIS and \hat{e}_z pointing towards the aperture of the telescope (“to Sky” direction in Fig. 2.1);

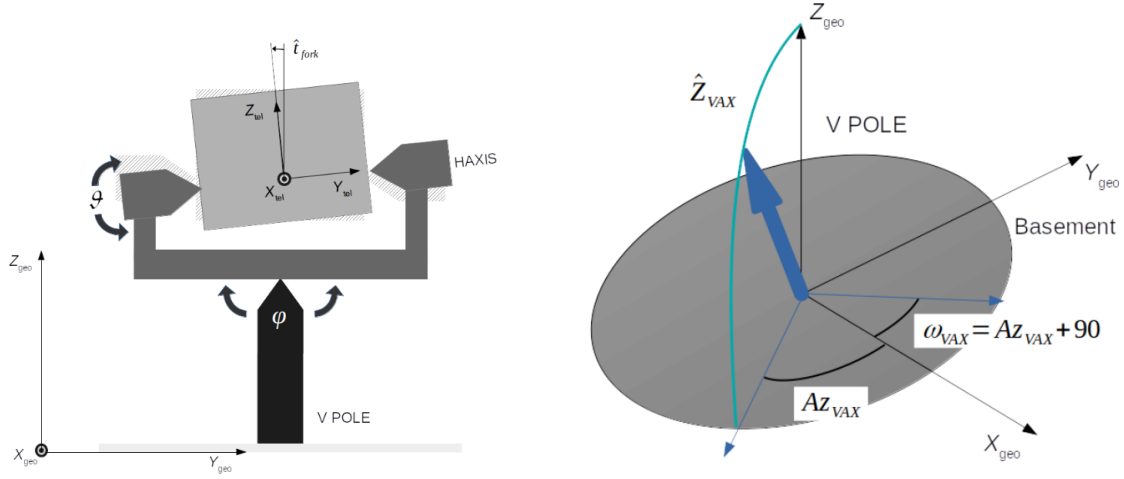


Figure 3.2: *Left:* fork representation with t_{fork} ; *Right:* flat base with wobble angles. Taken from [7]

- Camera r.f.: the origin is in the center of the detector (could be both the feedhorn or the star tracker) with \hat{e}_z normal to the camera plane and \hat{e}_x , \hat{e}_y aligned with the axis generating the camera plane.

For an ideal telescope at rest, with all the configuration angles and the control angles equal to zero, the three reference frames are aligned.

The pointing reconstruction method consists of project \hat{e}_z of the camera r.f. (i.e., the direction of sight of the detector) into the Topocentric r.f.; to do that one can use a chain of intrinsic rotation, every rotation is around a specific axis and defined by the following matrices:

$$\mathcal{R}_x(\alpha) = \begin{pmatrix} 1 & 0 & 0 \\ 0 & \cos \alpha & -\sin \alpha \\ 0 & \sin \alpha & \cos \alpha \end{pmatrix}, \quad (3.1)$$

$$\mathcal{R}_y(\alpha) = \begin{pmatrix} \cos \alpha & 0 & -\sin \alpha \\ 0 & 1 & 0 \\ \sin \alpha & 0 & \cos \alpha \end{pmatrix}, \quad (3.2)$$

$$\mathcal{R}_z(\alpha) = \begin{pmatrix} \cos \alpha & \sin \alpha & 0 \\ -\sin \alpha & \cos \alpha & 0 \\ 0 & 0 & 1 \end{pmatrix} \quad (3.3)$$

The final rotation chain could be split into three steps for clarity [7]:

$$\hat{\mathbf{P}}^{(\text{tel})} = \mathcal{R}_x(p_{\text{cam}})\mathcal{R}_y(t_{\text{cam}})\mathcal{R}_z(r_{\text{cam}}) \cdot \hat{e}_z^{\text{cam}} \quad (3.4)$$

$$\hat{\mathbf{P}}^{(\text{V-AXIS})} = \mathcal{R}_z(\varphi - \varphi_0)\mathcal{R}_x(t_{\text{fork}})\mathcal{R}_y(\theta - \theta_0) \cdot \hat{\mathbf{P}}^{(\text{tel})} \quad (3.5)$$

$$\hat{\mathbf{P}}^{(\text{topo})} = \mathcal{R}_{\text{wobble}}(z_{\text{Vax}}, \omega_{\text{Vax}}) \cdot \hat{\mathbf{P}}^{(\text{V-AXIS})} \quad (3.6)$$

where it is necessary to pay attention to $\mathcal{R}_{\text{wobble}}$ that is defined as a matrix representing a rotation of z_{Vax} around a generic axis; in this case the rotation axis is \hat{e}_x

rotated of ω_{Vax} around \hat{e}_z , i.e., the versor $\mathbf{u} = [\cos \omega_{\text{Vax}}, \sin \omega_{\text{Vax}}, 0]$. Explicitly, the rotation matrix is as follows:

$$\begin{aligned}\mathcal{R}_{\text{wobble}} &= \begin{pmatrix} \cos z_{\text{Vax}} + u_x^2(1 - \cos z_{\text{Vax}}) & u_x u_y (1 - \cos z_{\text{Vax}}) - u_z \sin z_{\text{Vax}} & u_x u_z (1 - \cos z_{\text{Vax}}) + u_y \sin z_{\text{Vax}} \\ u_y u_x (1 - \cos z_{\text{Vax}}) + u_z \sin z_{\text{Vax}} & \cos z_{\text{Vax}} + u_y^2(1 - \cos z_{\text{Vax}}) & u_y u_z (1 - \cos z_{\text{Vax}}) - u_x \sin z_{\text{Vax}} \\ u_z u_x (1 - \cos z_{\text{Vax}}) - u_y \sin z_{\text{Vax}} & u_z u_y (1 - \cos z_{\text{Vax}}) - u_x \sin z_{\text{Vax}} & \cos z_{\text{Vax}} + u_z^2(1 - \cos z_{\text{Vax}}) \end{pmatrix} \\ &= \begin{pmatrix} \cos z_{\text{Vax}} + u_x^2(1 - \cos z_{\text{Vax}}) & u_x u_y (1 - \cos z_{\text{Vax}}) & u_y \sin z_{\text{Vax}} \\ u_y u_x (1 - \cos z_{\text{Vax}}) & \cos z_{\text{Vax}} + u_y^2(1 - \cos z_{\text{Vax}}) & u_x \sin z_{\text{Vax}} \\ -u_y \sin z_{\text{Vax}} & -u_x \sin z_{\text{Vax}} & \cos z_{\text{Vax}} \end{pmatrix}\end{aligned}$$

in this way, ω_{Vax} doesn't rotate the reference frame, but it only represents the direction of the V-AXIS tilt.

The last step is to project $\hat{\mathbf{P}}^{(\text{topo})}$ into the Equatorial Celestial reference frame, using the position of LSPE/Strip (latitude, longitude, and height of the Teide Observatory) and the epoch of the measure (expressed for example through a Julian date). This last transformation has to take into account secondary effects like precession, nutation, aberration, and refraction; it is performed by standard astronomical packages (for example *Astropy* in Python or *AstroLib* in Julia). [9]

Part II

Simulations

Chapter 4

Simulations setup

In this chapter, I will present the setup and the methodology that I have adopted to simulate and reconstruct the pointing direction of LSPE/Strip and the error associated with any offsets in the *control angles*. Firstly, in Sec. 4.1 I will discuss the method to transform the observed time-ordered data (TOD) into a binned map; then, In Sec. 4.2 I will present the sky model that I have used as the observed signal from the telescope.

4.1 Simulation pipeline

In the first part of my thesis, I implemented the formalism introduced in Sec. 3.2 to simulate the non-idealities angles into *Stripeline*,¹ the official LSPE/Strip simulation pipeline written in *Julia*. I implemented the rotation chain described in Eq. 3.4 using quaternions instead of rotation matrices. In fact, every unit quaternion represents a rotation in a three-dimensional space: given a quaternion $\mathbf{q} = a + bi + cj + dk$ a rotation of an angle θ around a generic axis $\mathbf{u} = (u_x, u_y, u_z)$ can be written as:

$$\mathbf{q} = \cos \frac{\theta}{2} + (u_x \mathbf{i} + u_y \mathbf{j} + u_z \mathbf{k}) \sin \frac{\theta}{2} \quad (4.1)$$

where, for *Stripeline*, \mathbf{u} is one of the three Cartesian coordinate axes according to the rotation it must represent. Given a generic three-dimensional vector \mathbf{v} ,² applying a rotation (Eq. 4.1) is performed by evaluating the conjugation of \mathbf{q} and then:

$$\mathbf{v}_{\text{rotated}} = \mathbf{q} \mathbf{v} \mathbf{q}^{-1} \quad (4.2)$$

using the Hamiltonian product between quaternions. To encode the telescope's rotation chain, I used a composition of rotations by the consecutive product of all the quaternions representing the rotations in Eq. 3.4; then, I applied the resulting rotation quaternion $\mathbf{q} = q_0 + q_1 \mathbf{i} + q_2 \mathbf{j} + q_3 \mathbf{k}$ to the z-axis obtaining the final pointing direction:

$$\hat{\mathbf{P}}^{(\text{topo})} = \begin{bmatrix} 2(q_3 q_1 + q_0 q_2) \\ 2(q_2 q_3 - q_0 q_1) \\ 1 - 2(q_1^2 + q_2^2) \end{bmatrix}. \quad (4.3)$$

¹<https://github.com/lspesstrip/Stripeline.jl>

²It is always possible to represent a vector as a quaternion with *scalar part* equal to zero, i.e., $\mathbf{v} = 0 + bi + cj + dk$

Finally, the latter direction is projected into the Equatorial Celestial reference frame obtaining a tuple $(\theta_{\text{sky}}, \varphi_{\text{sky}})$ representing the co-latitude and the longitude of the direction in the sky.

4.1.1 TOD and binned maps

LSPE/Strip will observe the sky for two years following the scanning strategy described in Sec. 2.2; to fully reconstruct the observed signal in the sky, it is necessary to know at each time in which direction the telescope is pointing using the formalism described in Sec. 3.2-4.1. A problem arises when the *configuration angles* are not perfectly known, as this will cause a systematic error in the reconstructed pointing direction: the value measured at any given time will be recorded as seen as coming from an area of the sky that is displaced from the actually observed direction. To study the impact of this error, it is necessary to simulate an ideal reference case in which the angles are perfectly known, and then to compare the result with a perturbed case where some uncertainties are introduced. Without loss of generality, the reference case is the one in which all the *configuration angles* are zero; the perturbations, instead, are deviations from the reference case.

During its investigation, LSPE/Strip collects data with a certain sampling frequency ν : the signal coming from the sky is therefore measured at each time step $\Delta t = 1/\nu$. The final result of the observation is a timeline of data called TOD (Time Ordered Data); from this timeline it is then necessary, through the reconstruction of the pointing directions, to understand where the signal comes from at each moment in order to create a map in the sky. By associating the signal to a specific sky direction, the maps need a subdivision criterion into subdomains that identify the observed sky region: these subdomains are called pixels.

In my thesis, I have used *Healpix.jl* [15], a library that implements the HEALPix scheme to tessellate the sphere into pixels of equal area. The resolution of the map is specified using one parameter called N_{side} : the sphere is hierarchically tessellated into curvilinear quadrilaterals starting from a base of 12 pixels ($N_{\text{side}} = 1$), the resolution of the tessellation is increased by division of each pixel into four new ones (N_{side} indicates how many times the main pixel is divided, and it is a power of two).

The complete code used to generate the sky maps can be found on my GitHub page,³ here I report the pseudocode used to produce a map affected by a perturbed configuration angle:

- generate, using PySM, a Healpix sky maps to observe;
- for every time step Δt :
 - compute the pointing direction at time t affected by the systematic error;
 - estimate the expected signal along the pointing direction at time t ;
 - compute the ideal pointing direction;
 - given ideal direction find the corresponding ideal pixel;
 - assign the estimated value along the “wrong” direction to the ideal pixel;
- return the map with the observed sky.

³<https://github.com/teob97/PRMaps.jl>

Assuming that the signal is affected only by white noise, to convert the time-ordered data into a map I used the *binning* technique, consisting in computing the average value of the signal measured within each pixel of the sky. To save memory, observed signals aren't stored in a TOD, but the average is performed *on the fly* using the signal map and the hits map (containing the number of times that a pixel is observed).

4.2 Sky model

The observed sky signal is generated using PySM⁴ (v3.3.2) a Python code to generate full sky simulation of galactic foregrounds [14]. Each of the models is labeled with a letter and a number representing the emission kind and the model type. Since LSPE/Strip will observe only the polarization of the sky, I used only Q and U maps.

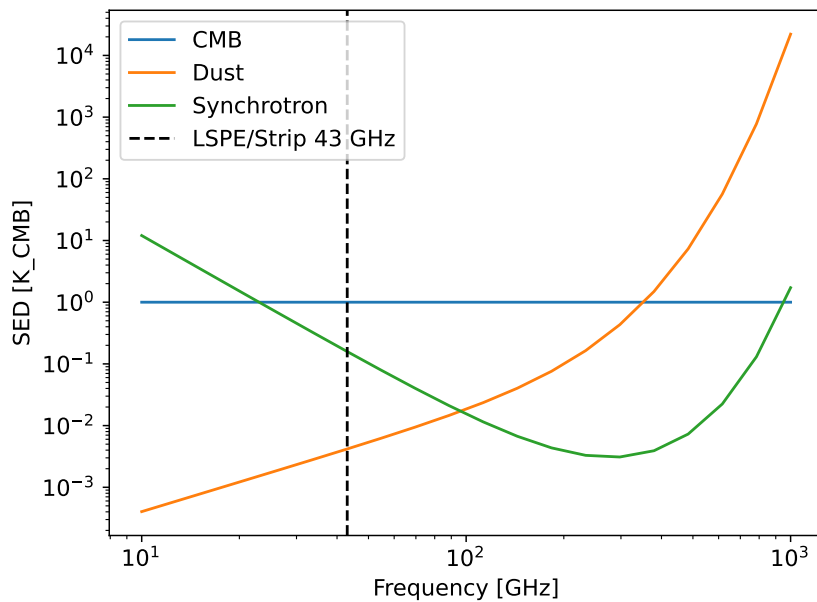


Figure 4.1: Spectral Energy Distribution (SED) of the foreground emissions.

4.2.1 CMB

Cosmic microwave background model “c1” is a lensed realization computed with Taylens,⁵ a Python library that uses nearest-neighbour Taylor interpolation [8].

4.2.2 Dust

Thermal dust emission is modeled as a *modified black body*. The model uses a 353 GHz template map in polarization estimated from the *Planck* data. The “d0”

⁴<https://github.com/galsci/pysm>

⁵<https://github.com/amaurea/taylens>

assumes a spatially fixed spectral index and a fixed black body temperature. Therefore, the spectral brightness can be represented by the following relation [14]:

$$\{Q_\nu^{\text{dust}}, U_\nu^{\text{dust}}\}(\hat{\mathbf{n}}) = \{A_Q, A_U\}(\hat{\mathbf{n}}) \times \left(\frac{\nu}{\nu_P}\right)^{\beta_d} B_\nu(T_d) \quad (4.4)$$

where β_d is the spectral index of the dust fixed to 1.54, T_d is the dust temperature fixed to 20 K, ν_P is the reference frequency in polarization equal to 353 GHz, A_U and A_Q are the amplitude of the U and Q stokes component and $B_\nu(T_d)$ is the black body spectrum at a temperature of T_d .

4.2.3 Synchrotron

Synchrotron radiation dominates for frequencies below 50 GHz, and it is the main signal that LSPE/Strip will handle. Model “s0” has a spectral brightness that is modeled as a power law with a spatially fixed spectral index equal to -3.0:

$$\{Q_\nu^{\text{synch}}, U_\nu^{\text{synch}}\}(\hat{\mathbf{n}}) = \{A_Q, A_U\}(\hat{\mathbf{n}}) \times \left(\frac{\nu}{\nu_0}\right)^{\beta_{\text{synch}}} \quad (4.5)$$

where ν_0 is the reference frequency of 23 GHz. In this case, the polarized signal is modeled as a scaling of the WMAP 9-year 23 GHz Q and U maps smoothed to three degrees.

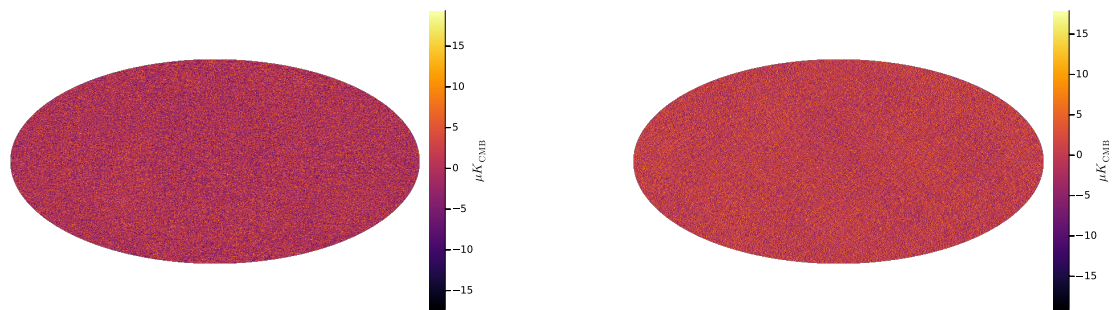


Figure 4.2: CMB signal at 43 GHz and $N_{\text{side}} = 512$. (*Left*: Q Stokes component; *Right*: U Stokes component)

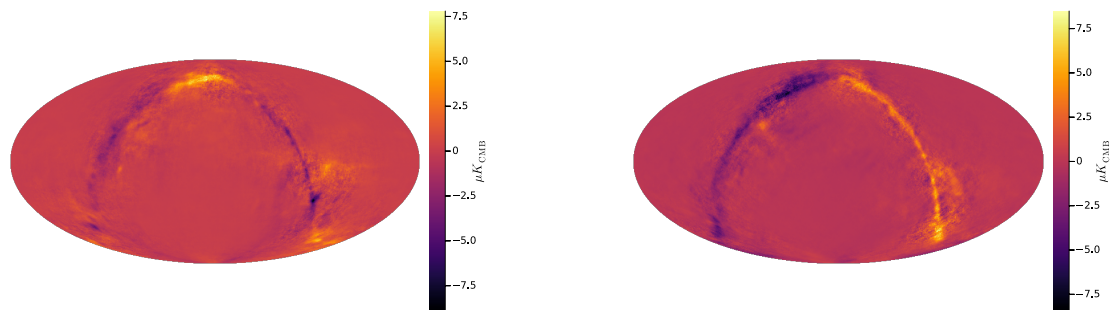


Figure 4.3: Dust signal at 43 GHz and $N_{\text{side}} = 512$. (*Left*: Q Stokes component; *Right*: U Stokes component)

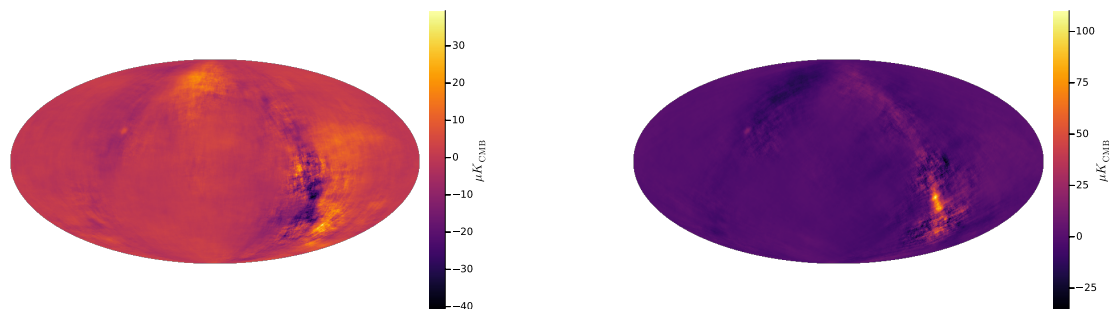


Figure 4.4: Synchrotron signal at 43 GHz and $N_{\text{side}} = 512$. (*Left*: Q Stokes component; *Right*: U Stokes component)

Chapter 5

Simulations results

Starting from the pipeline described in the previous chapter, I will present the first results that I obtained from the simulations. To study the impact of the systematic errors introduced in the configuration angles I undertook the following analysis: firstly, I estimated the error introduced in the pointing direction only, quantified as the angular difference (Sec. 5.1), then I went on to introduce a signal to be observed, and I studied how the pointing error distorted the observed sky (Sec. 5.3), it should be noted that in these simulations the Gaussian error due to instrumental sensitivity will not be considered; finally, in the next chapter I will present an analysis of the impact on the final scientific result. The entire pipeline is available on my GitHub page <https://github.com/teob97/Master-Thesis-Pipeline>.

5.1 Pointing accuracy

To choose the correct values to assign to the *configuration angles* during the simulation, I first had to study the impact of these angles on the final pointing direction. In this preliminary analysis, only the direction of sight is taken into account. The error is quantified using a metric defined as the angular difference between the effective direction $\hat{\mathbf{P}}$ and the ideal direction $\hat{\mathbf{P}}_{\text{ideal}}$ [7]:

$$\delta = \arccos(\hat{\mathbf{P}}_{\text{ideal}} \cdot \hat{\mathbf{P}}) \quad (5.1)$$

Since the required accuracy for LSPE/Strip is 30 arcsec, I tested all the *configuration angles* one by one using 30 arcsec, 1 arcmin, and 5 arcmin to quantify the trend of the error: in fact, the main purpose is to understand if it was possible to relax the requirement of 30 arcsec (especially regarding the accuracy of the star tracker).

I simulated the central horn for 5 days of observations (see Sec. 5.2) with a sampling frequency of 50 Hz: at each time step, I calculated the error with Eq. 5.1, and then I made an average over time. The results are reported in Fig. 5.1.

From the figure, it can be immediately deduced that the deviation in pointing is linearly proportional to the magnitude of the systematic error introduced on the single *configuration angle*. Furthermore, it is noted that the most problematic angles are the offset on the altitude motor and the fork angle, followed by the offset on the azimuth motor. As regards the wobble angles, the pointing error always remains below the requirement of 15 arcsec, which is the best-case scenario.

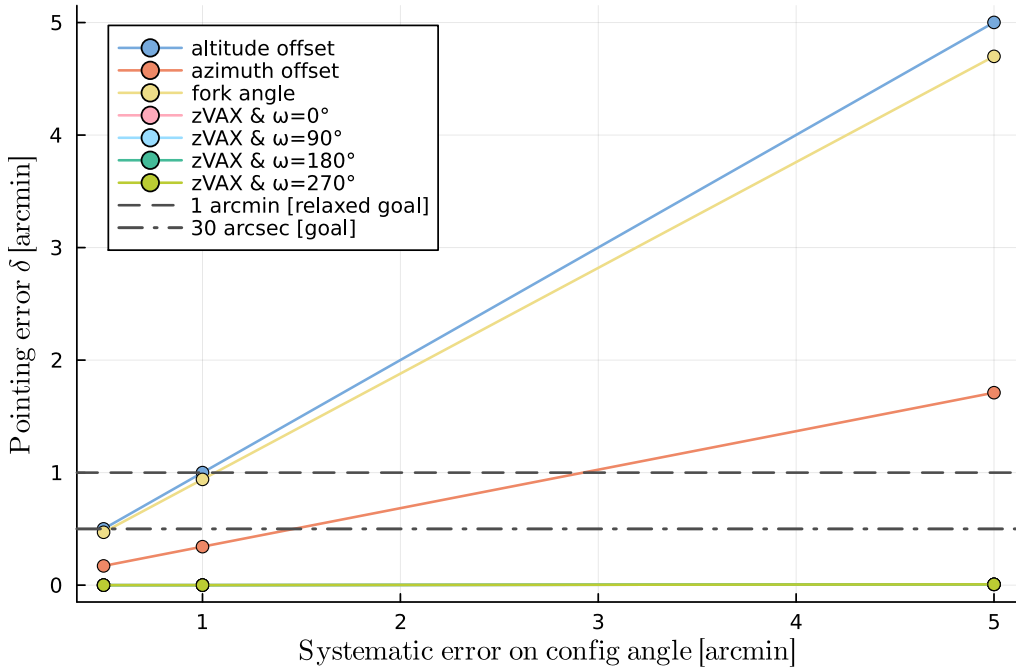


Figure 5.1: Pointing error as a function of the bias introduced in the different configuration angles.

5.2 Simulation duration

LSPE/Strip will observe the sky for two years, but from a simulation point of view, reproducing the entire survey would be too expensive. So I first investigated how pointing error varies over simulation time: I ran simulations with the following duration of [10, 50, 100, 200, 400, 600] days averaging the pointing error over the simulated days. Results are reported in Fig. 5.2.

As one would expect, the pointing error remains more or less unchanged over time: actually given the scanning strategy, once the pointing error has been calculated on a single turn of the telescope on itself (given that the strip of sky observed is a translation of the single circular pattern in the sky) the error will repeat the same, except for oscillations due to second order effects (such as recession, nutation, aberration, and refraction).

Assuming the presence of only uncorrelated Gaussian errors (see Sec. 6), a further factor to take into account is the binning technique for creating the maps: in fact, the more the observation time increases, the more a single pixel will be visited; consequently, given that the value in the single pixel is calculated as an average, the greater is the simulation time the smaller will be the error on the observed signal.

Given these results, I decided to adopt a duration of 10 days for the subsequent simulations, in order to minimize the computational cost and at the same time simulate the worst case: if the pointing accuracy prerequisites can be relaxed for this case, consequently they can be relaxed for the final two-year survey.

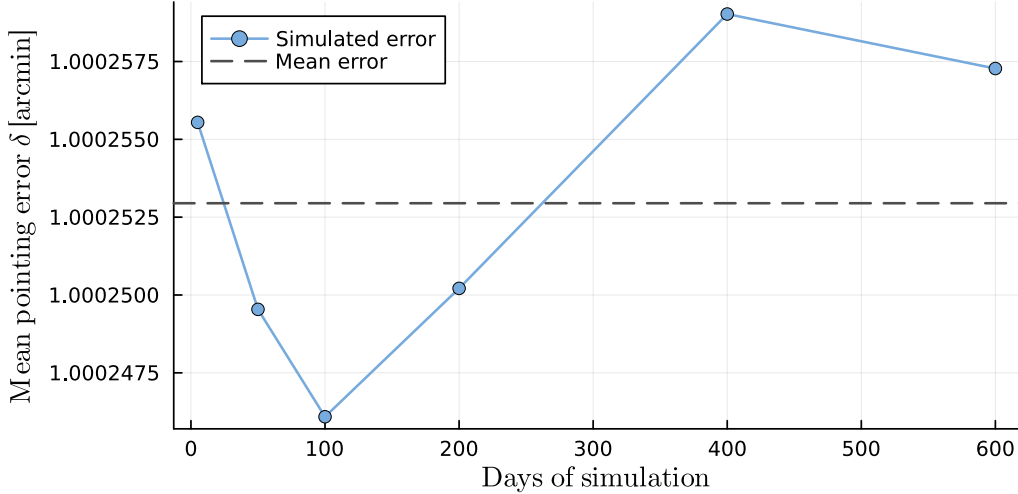


Figure 5.2: Mean pointing error as a function of the days of simulation. Configuration angle used: altitude offset [1 arcmin].

5.3 Noise maps and histograms

Once I decided the observation time to use (see Sec 5.2) and the magnitude of the error to introduce into the *configuration angles* (see Sec. 5.1) I carried out an analysis of the observed signal distortion caused by the pointing error. Here is the setup that I have used:

- only the central horn I0 with $(p_{\text{cam}}, t_{\text{cam}}, r_{\text{cam}}) = (0, 0, 0)$
- sky signal: \mathbf{s}_0 (only synchrotron) at 43 GHz
- sampling frequency: 50 Hz
- observation time: 10 days
- N_{side} : 512
- systematic error: 1 arcmin

I first simulated the ideal case map, i.e., with all the *configuration angles* equal to zero; after that, I introduced one angle at a time, a systematic error of 1 arcmin generating, also in this case, sky maps of the observed signal. About the wobble angles, the systematic error is introduced only in z_{Vax} , while ω_{Vax} (which indicates the direction at which the vertical axis is aimed) is set to coincide with the direction of the four cardinal points: therefore it will be $[0^\circ, 90^\circ, 180^\circ, 270^\circ]$.

Since LSPE/Strip will observe a polarized signal, I simulated only Q and U Stokes parameters and, in order to analyze the two data simultaneously, I decided to calculate the polarization, defined as $P = \sqrt{Q^2 + U^2}$, for every pixel of the maps. Then, I compared the ideal map with those affected by the systematic error by calculating the difference for each pixel between the ideal one and the one with the error. The maps I get, which I will call *noise maps*, represent the absolute error caused by pointing errors in the observed signal. As an example, in Fig. 5.3, I reported the result obtained for an offset of $\theta_0 = 1$ arcmin on the altitude angle.

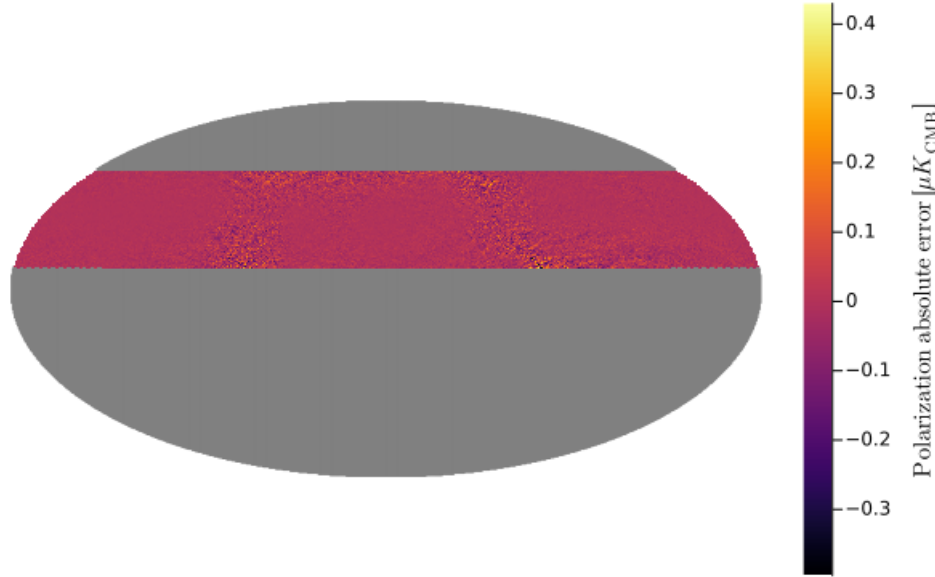


Figure 5.3: Noise map associated with an altitude offset of 1 arcmin.

It is possible to note that the error is more concentrated in the area where the galaxy is located, i.e., the area in which the synchrotron emission dominates at 43 GHz; this is because where the galaxy is located the signal has a greater gradient and therefore the sensitivity is greater. Here I report only the map obtained for the altitude offset (which is the one with the greatest incidence, see Sec. 5.1) as those for the other configuration angles are substantially similar and will be analyzed shortly by studying the distribution of the values associated with the pixels.

In fact, as anticipated, the next step of this analysis was to study how the pixel pointing error values are distributed: to do this I plotted the histogram corresponding to the various noise maps; in this way, it is possible to study the profile and quantify the width of the distribution to have a new parameter that estimates the severity of the error associated with the various *configuration angles*.

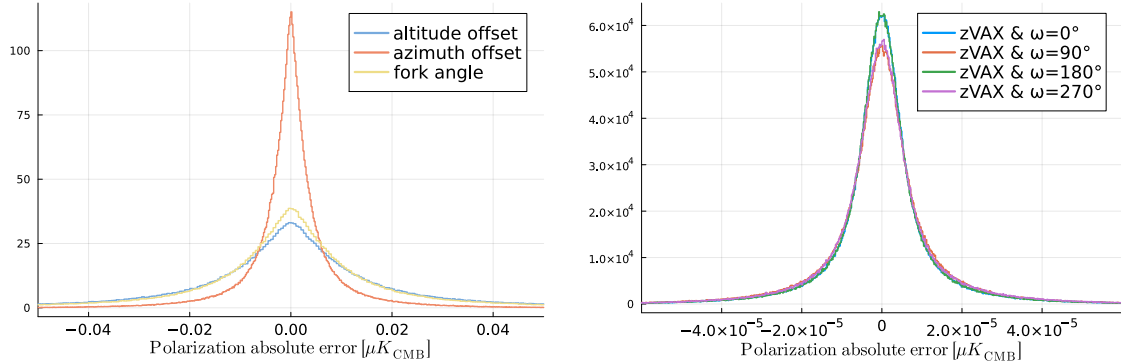


Figure 5.4: *Left:* histograms for altitude offset, azimuth offset, and fork angle. *Right:* the same histograms, but for the wobble angles. All configuration angle biases are 1 arcmin.

Histograms are plotted with the same binning (3000 bins) and individually normalized so that the total area of the bins is normalized to one. As reported in Fig. 5.4, for all the *configuration angles*, the histograms profile is symmetric and

centered in zero; however, it should be noted that the distribution is not Gaussian but, by making a fit it is found that it follows a Cauchy distribution:

$$f(x; \mu, \sigma) = \frac{1}{\pi\sigma \left(1 + \left(\frac{x-\mu}{\sigma}\right)^2\right)} \quad (5.2)$$

where μ is the *location parameter* and σ is the *scale parameter* which specifies the half-width at half-maximum (HWHM) of the distribution. Therefore, I decided to fit the distributions, obtaining for each one the two characteristic parameters, that I have reported in Table 5.1. This step is useful because we are able to have a precise estimate of the width of the distributions: in fact, using the standard deviation would have been an overestimation. I find once again that the most problematic parameter is the offset on the altitude angle, followed by the offset on the azimuth angle and the fork angle; as regards the wobble angles, the effect is orders of magnitude smaller than the previous ones. This data must be compared with the expected noise value per pixel: the instrumental sensitivity is $107 \mu\text{K}_{\text{CMB}}$ arcmin [1], this value, rescaled for a map with $N_{\text{side}} = 512$ becomes $\sigma \approx 15 \mu\text{K}_{\text{CMB}}$, the systematic error introduced by pointing is, therefore, orders of magnitude smaller than the noise.

	$\mu [\mu\text{K}]$	$\sigma [\mu\text{K}]$
Altitude offset	$9.81 \cdot 10^{-5}$	0.010
Azimuth offset	$3.70 \cdot 10^{-6}$	0.003
Fork angle	$1.52 \cdot 10^{-4}$	0.009
Wobble ($\omega=0$)	$1.88 \cdot 10^{-8}$	$4.750 \cdot 10^{-6}$
Wobble ($\omega=90$)	$1.70 \cdot 10^{-8}$	$5.434 \cdot 10^{-6}$
Wobble ($\omega=180$)	$-2.46 \cdot 10^{-8}$	$4.749 \cdot 10^{-6}$
Wobble ($\omega=270$)	$-1.57 \cdot 10^{-8}$	$5.304 \cdot 10^{-6}$

Table 5.1: Fitted location parameter μ and scale parameter σ for each *configuration angles*, assuming an error of 1 arcmin for each of them.

5.4 Error scaling

Finally, I have investigated how the error distribution scales as a function of the bias on the configuration angle. I ran the simulations with the same setup of the previous section, varying the value of the various configuration angles by using the following values [15, 30, 60, 300] arcsec.

Results are reported in Fig. 5.5. I computed the logarithm of the configuration angle and of the scale of the distribution: in fact, as can be seen from the figure, there is a linear relationship between these two quantities. I then fitted the data using a power law:

$$\log \sigma = a \log \alpha + b \quad (5.3)$$

where σ is the scale of the error distribution and α is the value associated with the *configuration angle*. The fitted parameters are reported in Table 5.2.

As was observed in the previous sections, in this case too, the most impacting errors on the configuration angles are the offsets on the altitude and azimuth motors

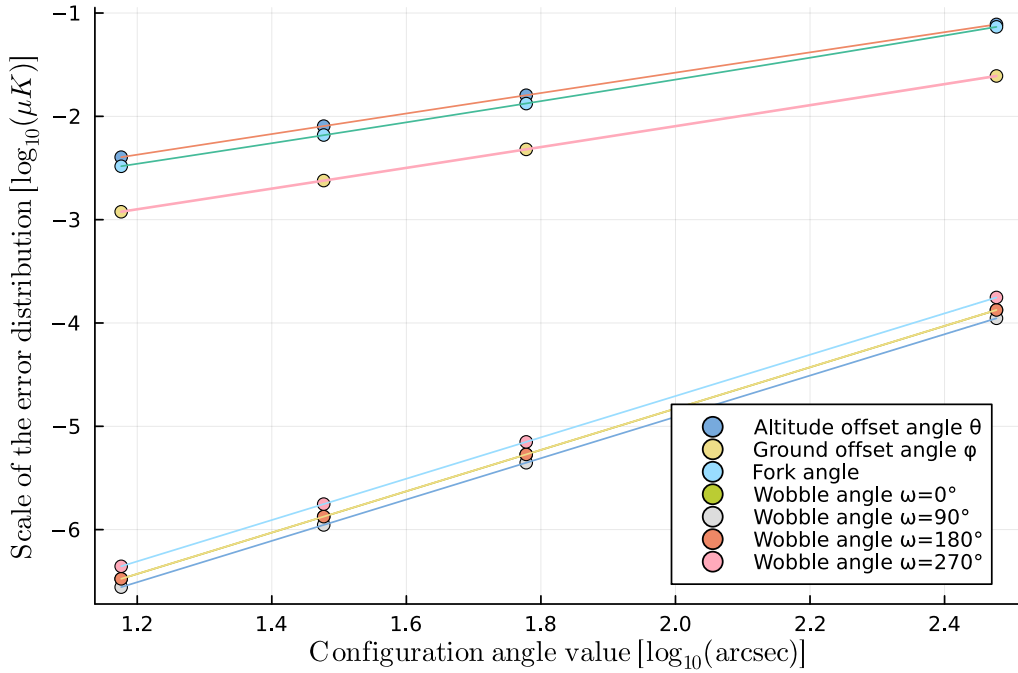


Figure 5.5: Width of the error distribution as a function of the bias introduced in the different configuration angles.

and the fork angle. Interestingly, the scaling law for the aforementioned angles is linear in good approximation (in fact $a \approx 1$), while for the wobble angles, we have a power law with an index approximately equal to 2. Fig. 5.5 shows that the wobble angles introduce an effect of orders of magnitude lower with respect to offsets and fork angles.

	a	b
Altitude offset	0.99	-3.55
Azimuth offset	1.01	-4.11
Fork angle	1.04	-3.71
Wobble ($\omega=0$)	2.00	-8.83
Wobble ($\omega=90$)	2.00	-8.91
Wobble ($\omega=180$)	2.00	-8.83
Wobble ($\omega=270$)	2.00	-8.71

Table 5.2: Equation 5.3 parameters fitted using data obtained from simulations.

Chapter 6

Component separation analysis

In this chapter, I am going to present the last analysis I have carried out: after having quantified the pointing error and having studied the effect on the observed signal (Ch. 5), I have examined the impact of the systematic pointing error on the reconstruction of the synchrotron spectrum of the portion of the sky that will be observed by LSPE/Strip.

The reason for this test is to investigate the effect of this kind of error in a case that is representative of the scientific use of LSPE/Strip data. Specifically, component separation is an indispensable step in the study of the CMB as it allows us to separate the signal we are interested in from the foreground signal such as dust and synchrotron, which would otherwise contaminate the final results. In my analysis, I used ForeGroundBuster¹ a Python library that performs a parametric component separation [13]: starting from a model of the foreground emissions and a set of sky maps at various frequencies, FGBuster fits the parameters of the input foreground emission spectra for each pixel.

Of course, instrumental white noise cause an error in the reconstruction of β_{synch} . This effect is worsened by the pointing inaccuracies I have reported in the previous chapter. As it is customary to neglect systematic error when their impact on science is below 10% of the effect of noise, I ran an analysis to assess their relative importance.

To have an accurate result it would be necessary to perform a Monte Carlo method on various noise realizations, nevertheless, I have carried out an analysis based on a single noise realization: since I will consider a constant synchrotron spectral index, my estimate for β_{synch} is already the average of all the observed pixels, and so, the result can be considered to be similar to a simple Monte Carlo simulation.

The sky model that I have chosen to use for my simulations is the one defined as `c1s0d0` in PySM, whose analytical form of the foreground spectrum is the one described in Sec. 4.2. However, I have introduced some constraints: the temperature and the spectral index of the dust are kept fixed at their nominal values, respectively $T_{\text{dust}} = 20$ K and $\beta_{\text{dust}} = 1.54$. In this way, the only parameters left to fit are the dust and synchrotron amplitudes and the synchrotron spectral index β_{synch} . The aim of this chapter is therefore to understand how the systematic error introduced in the pointing reconstruction affects the fit of the synchrotron index.

The component separation that I am going to carry out is therefore based on the

¹<https://github.com/fgbuster/fgbuster>

following assumptions: instrumental sensitivity is assumed to produce a Gaussian error; the sky area analyzed is only that covered by LSPE/Strip also for the frequencies associated with the other surveys used (Tab. 6.3); foreground parameters are assumed to be constant over the whole sky. The simulation pipeline can be summarized as follows:

- choose a set of instruments to simulate, i.e., the frequencies that will be used in the analysis;
- generate the sky maps at the above frequencies (only Q and U components) using PySM;
- run the pointing simulation (using Stripeline) to simulate the part of the sky that LSPE/Strip will observe;
- add Gaussian noise map to take into account the instrumental sensitivity;
- run FGBuster component separation.

As well as for the simulations of the previous chapter, these are available on the GitHub page <https://github.com/teob97/Master-Thesis-Pipeline>.

Once launched, FGBuster fits the value of the foreground parameters against the sky maps: to quantify the impact of the systematic pointing error with respect to the noise, it is necessary to introduce the following quantities:

$$\Delta\beta_{\text{point}} = \beta - \beta_{\text{ideal}} \quad (6.1)$$

$$\Delta\beta_{\text{noise}} = \beta_{\text{ideal}} - \beta_{\text{nominal}} \quad (6.2)$$

where β is the synchrotron index computed introducing a bias in one of the configuration angles, β_{ideal} is the one computed without pointing error (i.e., with all the configuration angles set to zero), and β_{nominal} is the nominal value used by PySM equal to -3.0 . I have quantified the impact of the pointing error as the ratio between the two quantities:

$$\eta \equiv \left| \frac{\Delta\beta_{\text{point}}}{\Delta\beta_{\text{noise}}} \right| \cdot 100. \quad (6.3)$$

This represents the percentage of β_{synch} distortion due to pointing error versus that due to instrumental noise. As mentioned above, for the pointing effect to be negligible it must be $\eta < 10\%$.

As with the previous chapter, I perturbed all the *configuration angles* individually and investigated whether it was possible to relax the pointing prerequisite by introducing a systematic error of $[0.5, 1.0, 5.0]$ arcmin. The setup of my simulations is the following:

- central horn I0 with $(p_{\text{cam}}, t_{\text{cam}}, r_{\text{cam}}) = (0, 0, 0)$
- sky signal: c1s0d0 (CMB, Synchrotron and Dust)
- sampling frequency: 50 Hz
- observation time: 10 days
- N_{side} : 128

I studied two sets of frequency coverages; the first assumes only frequencies measured by LSPE, and the second uses the standard set of maps usually employed in this kind of analysis (WMAP, Planck, ...).

6.1 Results using only LSPE

Firstly, I analyzed the case in which only the LSPE/Strip and LSPE/SWIPE channels are considered. Actually, for the parameter fit to be successful, I also had to add the 22.63 GHz WMAP channel and the 28.40 GHz Planck/LFI channel: LSPE/SWIPE frequencies are useful for reconstructing the dust, but, for this reason, to correctly characterize synchrotron (fitting β_{synch} and the amplitude A_{synch}) I decided to combine the two aforementioned channels of WMAP and Planck/LFI with LSPE/Strip at 43 GHz. The sensitivity of the instruments is reported in Tab. 6.3.

For the case with white noise but no pointing systematic, I obtained a value of $\Delta\beta_{\text{noise}} = -4.62997 \cdot 10^{-3}$. The results with different pointing systematics are reported in Tab. 6.1: the percentage error η (Eq.6.3) is shown in Fig. 6.1.

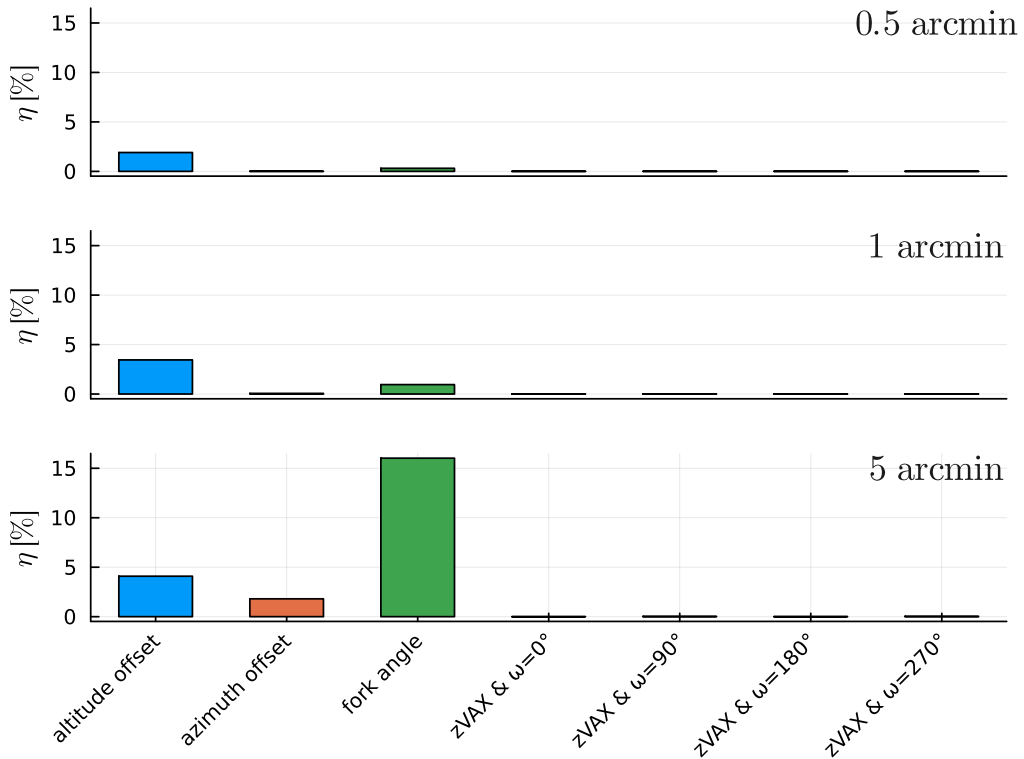


Figure 6.1: Percentage error η calculated for a bias in the configuration angles equal to [0.5, 1, 5] arcmin. These simulations only consider LSPE, Planck/LFI 30 GHz, and WMAP 23 GHz.

The impact of pointing error remains below the 10% threshold for uncertainties in the configuration angles of 1 arcmin, thus making it possible to relax the pointing prerequisite of 0.5 arcmin. If, on the other hand, we consider the case with 5 arcmin, the fork angle has a $\eta \approx 15\%$, beyond the required threshold. Thus, this is the most problematic angle, and it will require particular attention during the pointing calibration.

Configuration angle	Perturbation		
	0.5 arcmin	1 arcmin	5 arcmin
Altitude offset	-3.004718	-3.004790	-3.004819
Azimuth offset	-3.004630	-3.004627	-3.004546
Fork angle	-3.004620	-3.004586	-3.003888
Wobble angle ($\omega = 0^\circ$)	-3.004630	-3.004630	-3.004630
Wobble angle ($\omega = 90^\circ$)	-3.004630	-3.004630	-3.004629
Wobble angle ($\omega = 180^\circ$)	-3.004630	-3.004630	-3.004630
Wobble angle ($\omega = 270^\circ$)	-3.004630	-3.004630	-3.004632

Table 6.1: β_{synch} fitted using FGBuster with only the LSPE frequencies.

6.2 Results with other instruments

In this section, I show the results of a new set of simulations where all the “standard” measured CMB maps provided by the current literature are used: LSPE, WMAP, Planck, and Quijote (see Tab. 6.3 for the complete list of the instruments). The setup of the simulations is identical to that of the previous section. In this case, I have obtained $\Delta\beta_{\text{noise}} = -2.57514 \cdot 10^{-4}$, meaning that the impact of the white noise is one order of magnitude smaller with respect to the previous case with only LSPE. For this reason, it is legitimate to expect that the η values are much higher than in the previous case, since the denominator of Eq. 6.3 is much smaller. The fitted synchrotron spectral indexes for the configuration angles different from zero are reported in Tab. 6.2.

From the table, it can be seen that the discrepancy of beta with respect to the nominal case is an order of magnitude smaller than the previous case. While from Fig. 6.2, ignoring the higher percentages due to the smaller differences, it can be seen that now the most problematic angle is the altitude offset, reiterating what has already been found in the previous chapters.

Configuration angle	Perturbation		
	0.5 arcmin	1 arcmin	5 arcmin
Altitude offset	-3.0002704	-3.0002843	-3.0004372
Azimuth offset	-3.0002577	-3.0002579	-3.0002657
Fork angle	-3.0002573	-3.0002580	-3.0003058
Wobble angle ($\omega = 0^\circ$)	-3.0002575	-3.0002575	-3.0002575
Wobble angle ($\omega = 90^\circ$)	-3.0002575	-3.0002575	-3.0002574
Wobble angle ($\omega = 180^\circ$)	-3.0002575	-3.0002575	-3.0002576
Wobble angle ($\omega = 270^\circ$)	-3.0002575	-3.0002575	-3.0002577

Table 6.2: β_{synch} fitted using FGBuster with all the frequencies.

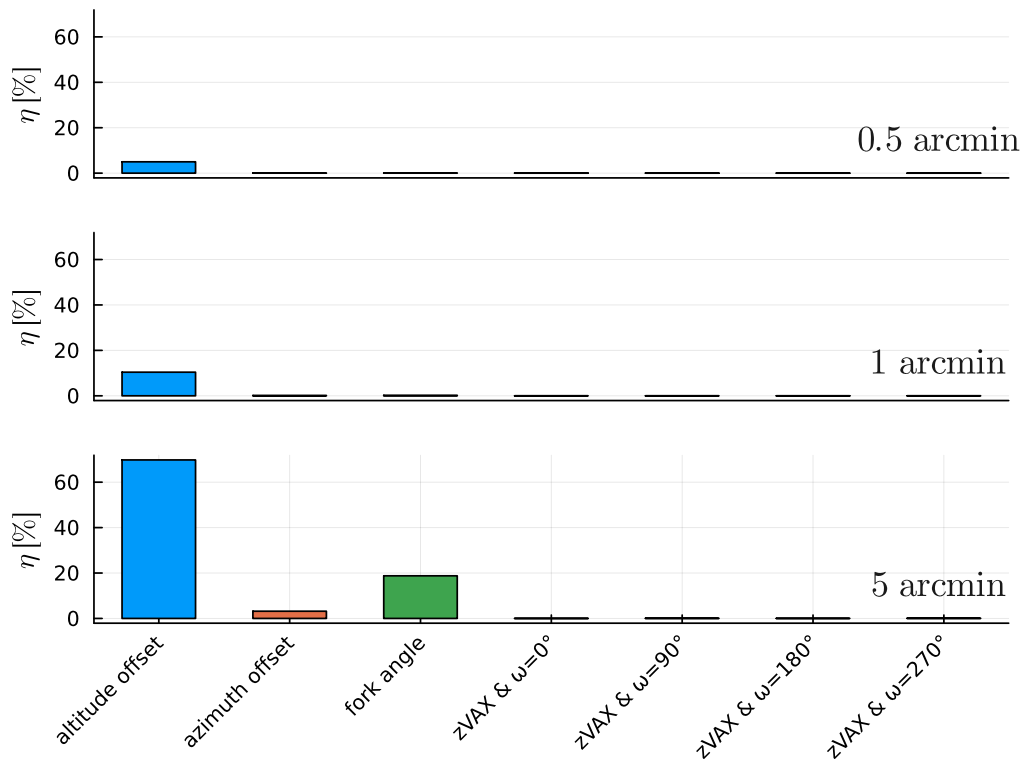


Figure 6.2: Percentage error η calculated for a bias in the configuration angles equal to [0.5, 1, 5] arcmin. These simulations consider all the instruments reported in Tab. 6.3.

Instruments	Freq. [GHz]	$\sigma_P [\mu K_{\text{CMB}} \text{ arcmin}]$	$\sigma_I [\mu K_{\text{CMB}} \text{ arcmin}]$
WMAP	22.69	294.70	293.47
WMAP	32.94	438.56	296.83
WMAP	40.72	500.99	415.02
WMAP	40.51	475.11	393.65
WMAP	60.09	554.72	520.19
WMAP	60.96	493.52	462.91
WMAP	92.87	783.58	750.75
WMAP	93.43	876.01	839.18
WMAP	92.44	926.76	887.75
WMAP	93.22	899.66	861.13
Planck/LFI	28.40	210.00	150.00
Planck/LFI	44.10	240.00	162.00
Planck/LFI	70.40	300.00	210.00
Planck/HFI	100.00	118.00	77.40
Planck/HFI	143.00	70.20	33.00
Planck/HFI	217.00	105.00	46.80
Planck/HFI	353.00	439.00	154.00
Quijote/MFT	11.00	1284.00	4254.00
Quijote/MFT	13.00	1122.00	3492.00
Quijote/MFT	17.00	966.00	5880.00
Quijote/MFT	17.00	1086.00	6204.00
Quijote/MFT	19.00	1314.00	6900.00
Quijote/MFT	19.00	1290.00	7320.00
LSPE/SWIPE	145.00	10.00	14.14
LSPE/SWIPE	210.00	17.00	24.04
LSPE/SWIPE	240.00	34.00	48.08
LSPE/Strip	43.00	102.00	144.25
LSPE/Strip	95.00	777.00	1098.84

Table 6.3: Parameters of the instruments used in my simulations.

Chapter 7

Conclusions

In my thesis, I have implemented and studied a pointing reconstruction model for the LSPE/Strip telescope that takes into account the uncertainties in the determination of the *configuration angles* which describes the telescope geometry. The goal was to quantify the impact of any systematic errors produced by uncertainties in the knowledge of those angles and study the possibility of relaxing the pointing accuracy prerequisite from 30 arcsec to 1 arcmin.

After having found a linear relationship between the bias introduced in the configuration angles and the actual deviation in the pointing direction, I analyzed the impact that this systematic error produces on the celestial signal observed by the telescope. I found that the width of the absolute error distribution scales linearly for the offsets and for the fork angle, while it scales as a power law for the wobble angles. From a qualitative point of view, the configuration angles whose uncertainties would introduce a greater error are the offset and the fork angle. However, the error introduced turns out to be, in the worst case, of the order of $10^{-3}\mu\text{K}$ for uncertainties of the order of 1 arcmin, i.e., orders of magnitude smaller than the noise given by the instrumental sensitivity.

As a case of a representative scientific use of LSPE/Strip data I carried out a parametric component separation using ForeGroundBuster: in fact, it is necessary that LSPE/Strip, having among its primary objectives the characterization of the synchrotron signal, is able to provide useful data to extrapolate the parameters of the foregrounds. I studied both the case with only the frequencies covered by LSPE and the case with also the frequencies covered by the previous surveys, then I fitted the synchrotron spectral index both in an ideal case and by introducing biases in the configuration angles. As a criterion, a systematic effect is negligible if its effect is below 10% of the effect of noise.

The results show that for configuration angle uncertainties of the order of 1 arcmin, the effect of the pointing error is actually less than 10% with respect to the noise. This tells us, as a final result, that the pointing accuracy prerequisite can be relaxed up to 1 arcmin. The pointing accuracy of the order of 1 arcmin is also comparable with that achieved by other surveys such as Quijote/MFI [12].

As far as future developments are concerned, using greater computing power than the one at my disposal, the same analysis could be re-run by simulating a complete two-year survey with all the active horns and carrying out the component separation no longer on a single noise realization but to exploit a Monte Carlo method to have a statistically more robust result. It is also possible to complicate the setup: in

the observed sky, for example, it is possible to use a synchrotron model with a direction-dependent index, in order to further investigate the distortions caused by a possible systematic error; and then, the geometric model of the telescope will also be complicated, introducing time-dependent *configuration angles* and therefore aging effects or second-order effects such as flexures.

Appendix A

Linearization

In this appendix, I will present a possible method to linearize the rotation operator used to reconstruct the pointing. Given the operator:

$$\mathcal{A} = \mathcal{R}_z(\omega_{\text{Vax}})\mathcal{R}_x(z_{\text{Vax}})\mathcal{R}_z(\varphi - \varphi_0)\mathcal{R}_x(t_{\text{fork}})\mathcal{R}_y(\theta - \theta_0)\mathcal{R}_x(p_{\text{cam}})\mathcal{R}_y(t_{\text{cam}})\mathcal{R}_z(r_{\text{cam}}) \quad (\text{A.1})$$

representing the rotation chain, it is possible to linearize it by expanding every rotation matrix at the first order using the following base:

$$\delta_X = \begin{bmatrix} 0 & 0 & 0 \\ 0 & 0 & -1 \\ 0 & 1 & 0 \end{bmatrix}, \delta_Y = \begin{bmatrix} 0 & 0 & 1 \\ 0 & 0 & 0 \\ -1 & 0 & 0 \end{bmatrix}, \delta_Z = \begin{bmatrix} 0 & -1 & 0 \\ 1 & 0 & 0 \\ 0 & 0 & 0 \end{bmatrix} \quad (\text{A.2})$$

The generic rotation matrices approximated at the first order becomes:

$$\mathcal{R}_x(\alpha) = I + \alpha\delta_X \quad (\text{A.3})$$

$$\mathcal{R}_y(\alpha) = I + \alpha\delta_Y \quad (\text{A.4})$$

$$\mathcal{R}_z(\alpha) = I + \alpha\delta_Z \quad (\text{A.5})$$

Now, I introduce the rotation matrix associated to the wobble angles rotation, starting from a generic matrix (see Sec.3.2), representing a rotation by an angle z around a generic axis $\mathbf{u} = [u_x, u_y, u_z]$. In our case, u is the versor corresponding to the x-axis rotated by an angle equal to ω , we can approximate to the first order ($\cos z \approx 1$, $\sin z \approx z$):

$$R_{\text{wobble}} \approx \begin{bmatrix} 1 & -u_x \cdot z & u_y \cdot z \\ u_z \cdot z & 1 & -u_x \cdot z \\ -u_y \cdot z & u_x \cdot z & 1 \end{bmatrix} = I + zu_x \cdot \delta_X + zu_y \cdot \delta_Y + zu_z \cdot \delta_Z \quad (\text{A.6})$$

In this case $u = [\cos \omega, \sin \omega, 0]$:

$$R_{\text{wobble}} = I + z \cos \omega \cdot \delta_X + z \sin \omega \cdot \delta_Y \quad (\text{A.7})$$

Then, it is possible also to approximate the offset angles associated with the motor angles ($\varphi_0 \approx 0$, $\theta_0 \approx 0$):

$$R_{\text{ground}} = \mathcal{R}_z(\varphi - \varphi_0) \approx \mathcal{R}_z(\varphi)(1 - \varphi_0\delta_Z) \quad (\text{A.8})$$

$$R_{\text{altitude}} = \mathcal{R}_y(\theta - \theta_0) \approx \mathcal{R}_y(\theta)(1 - \theta_0\delta_Y) \quad (\text{A.9})$$

Equation A.1 became:

$$\begin{aligned}\mathcal{A} \approx & (I + z_{\text{Vax}} \cos \omega_{\text{Vax}} \cdot \delta_X + z_{\text{Vax}} \sin \omega_{\text{Vax}} \cdot \delta_Y) \cdot \\ & \mathcal{R}_z(\varphi)(1 - \varphi_0 \delta_Z)(I + t_{\text{fork}} \delta_X) \mathcal{R}_y(\theta)(1 - \theta_0 \delta_Y) \cdot \\ & (I + p_{\text{cam}} \delta_X)(I + t_{\text{cam}} \delta_Y)(I + r_{\text{cam}} \delta_Z)\end{aligned}\quad (\text{A.10})$$

Now I do all the multiplication, keeping only the first order terms, and taking into account the fact that rotation matrix doesn't commute:

$$\begin{aligned}\mathcal{A} \approx & (I + z_{\text{Vax}} \cos \omega_{\text{Vax}} \cdot \delta_X + z_{\text{Vax}} \sin \omega_{\text{Vax}} \cdot \delta_Y) \cdot \\ & \mathcal{R}_z(\varphi)(1 - \varphi_0 \delta_Z + t_{\text{fork}} \delta_X - \theta_0 \delta_Y) \mathcal{R}_y(\theta) \cdot \\ & (I + p_{\text{cam}} \delta_X + t_{\text{cam}} \delta_Y + r_{\text{cam}} \delta_Z) \\ = & \mathcal{R}_z(\varphi)[I + z_{\text{Vax}} \cos \omega_{\text{Vax}} \cdot \mathcal{R}_z(\varphi)^T \delta_X \mathcal{R}_z(\varphi) + z_{\text{Vax}} \sin \omega_{\text{Vax}} \cdot \mathcal{R}_z(\varphi)^T \delta_Y \mathcal{R}_z(\varphi)] \cdot \\ & (I + p_{\text{cam}} \mathcal{R}_y(\theta) \delta_X \mathcal{R}_y(\theta)^T + t_{\text{cam}} \mathcal{R}_y(\theta) \delta_Y \mathcal{R}_y(\theta)^T + r_{\text{cam}} \mathcal{R}_y(\theta) \delta_Z \mathcal{R}_y(\theta)^T) \mathcal{R}_y(\theta)\end{aligned}$$

At this point, we can evaluate the terms with the transposed matrices:

$$\begin{aligned}\mathcal{R}_z(\alpha)^T \delta_X \mathcal{R}_z(\alpha) &= \begin{bmatrix} 0 & 0 & \sin \alpha \\ 0 & 0 & -\cos \alpha \\ -\sin \alpha & \cos \alpha & 0 \end{bmatrix} = \cos \alpha \delta_X + \sin \alpha \delta_Y \\ \mathcal{R}_z(\alpha)^T \delta_y \mathcal{R}_z(\alpha) &= \begin{bmatrix} 0 & 0 & \cos \alpha \\ 0 & 0 & \sin \alpha \\ -\cos \alpha & \sin \alpha & 0 \end{bmatrix} = -\sin \alpha \delta_X + \cos \alpha \delta_Y \\ \mathcal{R}_y(\alpha) \delta_X \mathcal{R}_y(\alpha)^T &= \cos \alpha \delta_X + \sin \alpha \delta_Z \\ \mathcal{R}_y(\alpha) \delta_Z \mathcal{R}_y(\alpha)^T &= -\sin \alpha \delta_X + \cos \alpha \delta_Z\end{aligned}$$

Now it is possible to rewrite the operator in this way:

$$\begin{aligned}\mathcal{A} \approx & \mathcal{R}_z(\varphi)[I + z_{\text{Vax}} \cos \omega_{\text{Vax}} \cdot (\cos \varphi \cdot \delta_X + \sin \varphi \cdot \delta_Y) + \\ & z_{\text{Vax}} \sin \omega_{\text{Vax}} \cdot (-\sin \varphi \cdot \delta_X + \cos \varphi \cdot \delta_Y)] \cdot \\ & [I + p_{\text{cam}}(\cos \theta \cdot \delta_X + \sin \theta \cdot \delta_Z) + t_{\text{cam}} \delta_Y + r_{\text{cam}}(-\sin \theta \cdot \delta_X + \cos \theta \cdot \delta_Z)] \mathcal{R}_y(\theta) \\ = & \mathcal{R}_z(\varphi)[I + z_{\text{Vax}} \cos \omega_{\text{Vax}} \cdot (\cos \varphi \cdot \delta_X + \sin \varphi \cdot \delta_Y) + \\ & z_{\text{Vax}} \sin \omega_{\text{Vax}} \cdot (-\sin \varphi \cdot \delta_X + \cos \varphi \cdot \delta_Y) + \\ & p_{\text{cam}}(\cos \theta \cdot \delta_X + \sin \theta \cdot \delta_Z) + t_{\text{cam}} \delta_Y + r_{\text{cam}}(-\sin \theta \cdot \delta_X + \cos \theta \cdot \delta_Z)] \mathcal{R}_y(\theta)\end{aligned}$$

Grouping similar terms, I obtain the linearized version of the rotation chain:

$$\mathcal{A} \approx \mathcal{R}_z(\varphi) \cdot [I + A \delta_X + B \delta_Y + C \delta_Z] \cdot \mathcal{R}_y(\theta)$$

with

$$A = t_{\text{fork}} + z_{\text{Vax}} \cos(\omega_{\text{Vax}} + \varphi) + p_{\text{cam}} \cos \theta - r_{\text{cam}} \sin \theta \quad (\text{A.11})$$

$$B = -\theta_0 + t_{\text{cam}} + z_{\text{Vax}} \sin(\omega_{\text{Vax}} + \varphi) \quad (\text{A.12})$$

$$C = -\varphi_0 + p_{\text{cam}} \sin \theta + r_{\text{cam}} \cos \theta \quad (\text{A.13})$$

Bibliography

- [1] G. Addamo et al. “The large scale polarization explorer (LSPE) for CMB measurements: performance forecast”. In: *Journal of Cosmology and Astroparticle Physics* 2021.08 (Aug. 2021), p. 008. DOI: [10.1088/1475-7516/2021/08/008](https://doi.org/10.1088/1475-7516/2021/08/008). URL: <https://doi.org/10.1088/1475-7516/2021/08/008>.
- [2] M. Bersanelli et al. “A coherent polarimeter array for the Large Scale Polarization Explorer (LSPE) balloon experiment”. In: (Sept. 2012). Ed. by Ian S. McLean, Suzanne K. Ramsay, and Hideki Takami. DOI: [10.1111/12.925688](https://doi.org/10.1111/12.925688). URL: <https://doi.org/10.1111/12.925688>.
- [3] N. W. Boggess et al. “The COBE Mission: Its Design and Performance Two Years after Launch”. In: *Astrophysical Journal* 397 (Oct. 1992), p. 420. DOI: [10.1086/171797](https://doi.org/10.1086/171797).
- [4] Wendy L. Freedman. “Cosmology at a crossroads”. In: *Nature Astronomy* 1, 0121 (May 2017), p. 0121. DOI: [10.1038/s41550-017-0121](https://doi.org/10.1038/s41550-017-0121).
- [5] Edwin Hubble. “A Relation between Distance and Radial Velocity among Extra-Galactic Nebulae”. In: *Proceedings of the National Academy of Science* 15.3 (Mar. 1929), pp. 168–173. DOI: [10.1073/pnas.15.3.168](https://doi.org/10.1073/pnas.15.3.168).
- [6] Federico Incardona. “Observing the polarized Cosmic Microwave Background from the Earth: scanning strategy and polarimeters test for the LSPE/STRIP instrument”. en. In: (2020). DOI: [10.13130/INCARDONA-FEDERICO_PHD2020-01-17](https://hdl.handle.net/2434/701276). URL: <http://air.unimi.it/handle/2434/701276>.
- [7] Michele Maris et al. *STRIP/LSPE: Pointing Reconstruction Model*. Technical note LSPE-STRIP-SP-028. Dec. 2021.
- [8] Sigurd K Næss and Thibaut Louis. “Lensing simulations by Taylor expansion — not so inefficient after all”. In: *Journal of Cosmology and Astroparticle Physics* 2013.09 (Sept. 2013), pp. 001–001. DOI: [10.1088/1475-7516/2013/09/001](https://doi.org/10.1088/1475-7516/2013/09/001). URL: <https://doi.org/10.1088/1475-7516/2013/09/001>.
- [9] U. S. Naval Observatory. *The Astronomical Almanac*. URL: https://aa.usno.navy.mil/publications/exp_supp.
- [10] A. A. Penzias and R. W. Wilson. “A Measurement of Excess Antenna Temperature at 4080 Mc/s.” In: *The Astrophysical Journal* 142 (July 1965), pp. 419–421. DOI: [10.1086/148307](https://doi.org/10.1086/148307).
- [11] Planck Collaboration et al. “Planck 2018 results - VI. Cosmological parameters”. In: *A&A* 641 (2020), A6. DOI: [10.1051/0004-6361/201833910](https://doi.org/10.1051/0004-6361/201833910). URL: <https://doi.org/10.1051/0004-6361/201833910>.

- [12] J A Rubiño-Martín et al. “QUIJOTE scientific results – IV. A northern sky survey in intensity and polarization at 10–20 GHz with the multifrequency instrument”. In: *Monthly Notices of the Royal Astronomical Society* 519.3 (Jan. 2023), pp. 3383–3431. ISSN: 0035-8711. DOI: [10.1093/mnras/stac3439](https://doi.org/10.1093/mnras/stac3439). eprint: <https://academic.oup.com/mnras/article-pdf/519/3/3383/48601065/stac3439.pdf>. URL: <https://doi.org/10.1093/mnras/stac3439>.
- [13] Radek Stompor et al. “Maximum likelihood algorithm for parametric component separation in cosmic microwave background experiments”. In: *Monthly Notices of the Royal Astronomical Society* 392.1 (Dec. 2008), pp. 216–232. ISSN: 0035-8711. DOI: [10.1111/j.1365-2966.2008.14023.x](https://doi.org/10.1111/j.1365-2966.2008.14023.x). eprint: <https://academic.oup.com/mnras/article-pdf/392/1/216/3707574/mnras0392-0216.pdf>. URL: <https://doi.org/10.1111/j.1365-2966.2008.14023.x>.
- [14] B. Thorne et al. “The Python Sky Model: software for simulating the Galactic microwave sky”. In: *Monthly Notices of the Royal Astronomical Society* 469.3 (May 2017), pp. 2821–2833. DOI: [10.1093/mnras/stx949](https://doi.org/10.1093/mnras/stx949). URL: <https://doi.org/10.1093/mnras/stx949>.
- [15] Maurizio Tomasi and Zack Li. *Healpix.jl: Julia-only port of the HEALPix library*. Version 3.0. Sept. 2021. ascl: [2109.028](https://ui.adsabs.harvard.edu/abs/2021ascl.soft09028T). URL: <https://ui.adsabs.harvard.edu/abs/2021ascl.soft09028T>.
- [16] M. Tristram et al. “Planck constraints on the tensor-to-scalar ratio”. In: *Astronomy & Astrophysics* 647 (Mar. 2021), A128. DOI: [10.1051/0004-6361/202039585](https://doi.org/10.1051/0004-6361/202039585). URL: <https://doi.org/10.1051/0004-6361/202039585>.